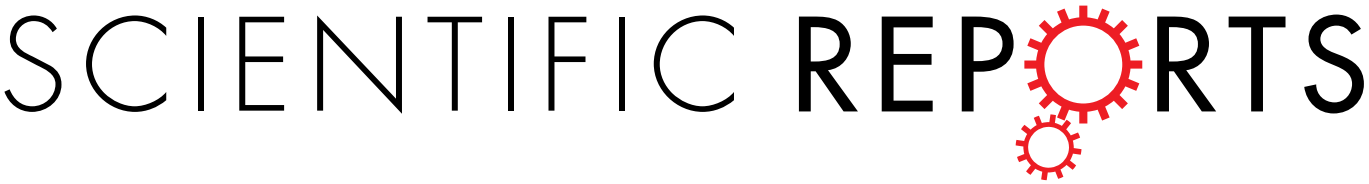

OPEN

Significant Performance Enhancement in Asymmetric Supercapacitors based on Metal Oxides, Carbon nanotubes and Neutral Aqueous Electrolyte

Received: 23 April 2015
Accepted: 21 July 2015
Published: 23 October 2015

Arvinder Singh & Amreesh Chandra

Amongst the materials being investigated for supercapacitor electrodes, carbon based materials are most investigated. However, pure carbon materials suffer from inherent physical processes which limit the maximum specific energy and power that can be achieved in an energy storage device. Therefore, use of carbon-based composites with suitable nano-materials is attaining prominence. The synergistic effect between the pseudocapacitive nanomaterials (high specific energy) and carbon (high specific power) is expected to deliver the desired improvements. We report the fabrication of high capacitance asymmetric supercapacitor based on electrodes of composites of SnO_2 and V_2O_5 with multiwall carbon nanotubes and neutral 0.5 M Li_2SO_4 aqueous electrolyte. The advantages of the fabricated asymmetric supercapacitors are compared with the results published in the literature. The widened operating voltage window is due to the higher over-potential of electrolyte decomposition and a large difference in the work functions of the used metal oxides. The charge balanced device returns the specific capacitance of ~198 F g^{-1} with corresponding specific energy of ~89 Wh kg^{-1} at 1 A g^{-1}. The proposed composite systems have shown great potential in fabricating high performance supercapacitors.

There is a growing demand to bring a step change in the specific power and energy delivered by supercapacitors. Such increase, along with the intrinsic advantage of fast charging/discharging rates, long cycle life (>10,000 cycles), and wide operational temperature range will allow the supercapacitors to compete with Li-ion batteries[1]. High performance supercapacitors have the capability to become an integral component of hybrid electric vehicles, back-up power supplies, mobiles, laptops, video cameras, signal transmitters, wearable electronics, etc.[2]. The specific energy (E) of supercapacitors can be enhanced by increasing the operating voltage window (V) and/or capacitance (C) as $E = \frac{1}{2}CV^2$. Consequently, supercapacitors employing ionic liquids or acetonitrile based electrolytes with operational voltage in the range 3-4 V have been reported[3,4]. However, the limited specific power and toxicity of these supercapacitors are the major limiting factors[5,6]. Aqueous electrolytes can be used as an alternative to their non-aqueous counterparts with an issue of narrow operating voltage window (~1.2 V), which mostly obstructs the specific energy of SCs[7,8]. Therefore, the fabrication of asymmetric supercapacitors (ASCs) in aqueous electrolytes is attaining more prominence to expand the operating voltage window. In ASCs, the implementation of the two appropriate electrode materials in the same electrolyte can add together their overlapped/non-overlapped operating voltage window. Therefore, an asymmetric cell configuration with

Department of Physics, Indian Institute of Technology Kharagpur, Kharagpur-721302, West Bengal, India. Correspondence and requests for materials should be addressed to A.C. (email: achandra@phy.iitkgp.ernet.in)

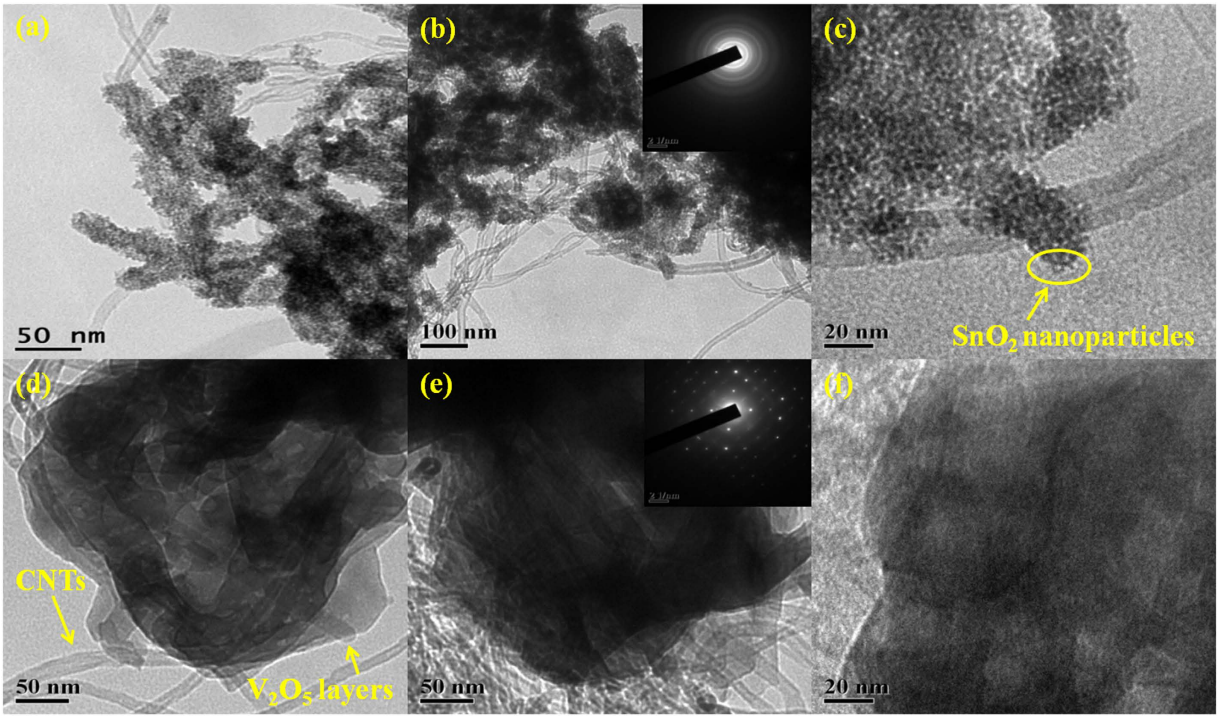

Figure 1. TEM micrographs for (**a–c**) MWS; (**d–f**) MWV composite.

correctly charge-balanced electrodes endows ASCs with the advantage of an extended cell voltage and high specific energy[9].

Supercapacitors with reasonably high specific capacitance values are being fabricated using nano-sized transition metal oxides (e.g., MnO_2, SnO_2, Fe_3O_4, MoO_3, V_2O_5 etc.)[10–16]. However, the low electrical conductivity of these metal oxides undermines their cyclic stability and limits the specific power that can be extracted. Consequently, use of composites with conventional carbon based materials having high electrical conductivity, surface area, chemical and mechanical stability is being[17–19]. The specific energy and coulombic efficiencies of such supercapacitors are predominantly decided by the characteristics of the electroactive material (EAM) taking part in the redox processes. The loss of performance is directly linked to the low capacitive negative electrode materials[20,21].

Presently, amongst the various oxides being investigated as electrode material, tin (IV) oxide is cost-effective with good electrochemical response and easy synthesis[22,23]. Similarly, nanostructures of vanadium (V, IV) oxide are explored as pseudocapacitive materials due to their high physical and chemical stability[24,25]. In this paper, it is shown that the synergistic effect of MWCNTs with electroactive materials SnO_2 and V_2O_5 can lead to appreciable increase in the specific capacitance. The charge balanced device assembled in 0.5 M Li_2SO_4 can be operated up to 1.8 V with no signature of gaseous evolution at upper bound of the potential. This allows the device to reach the maximum specific capacitance of ~198 F g^{-1} and specific energy of ~89 Wh kg^{-1}. The fabricated ASCs also show good rate capability and retain ~96% of their initial specific capacitance value, even after 1200 cycles at 2 A g^{-1} charging/discharging current. The reasons contributing to the enhancement of specific energy are explained using the relevant theoretical models.

Results

Physical characterizations. Figure 1a–c shows the high resolution transmission electron microscopy (TEM) micrographs of the composite systems. From the TEM micrographs, it can be seen that spherical SnO_2 nanoparticles and layered V_2O_5 are uniformly dispersed in the MWCNTs (MW) matrix. The elemental mapping shown in supplementary Fig. S1 confirms this inference. Supplementary Fig. S2 depicts FESEM micrographs for MWCNTs/SnO_2 (MWS) and MWCNTs/V_2O_5 (MWV) whereas supplementary Fig. S3 shows the FESEM and TEM micrographs of spherical SnO_2 nanoparticles and V_2O_5. It is important to mention that the phase formation, chemical state, and nature of bonding associated with the metal oxide were determined using the standard analysis of X-ray diffraction (Supplementary Fig. S4), X-ray photoelectron spectroscopy (XPS) (Supplementary Fig. S5), Fourier transform infrared spectroscopy (FTIR) and thermogravimetric analysis (TGA) (Supplementary Fig. S6) data. The details are given in the supplementary data.

The adsorption and desorption isotherms observed for the MWS composite was similar to IV-type isotherm with H3 hysteresis suggesting meso-porosity with capillary pore structures (see Fig. 2a). Using

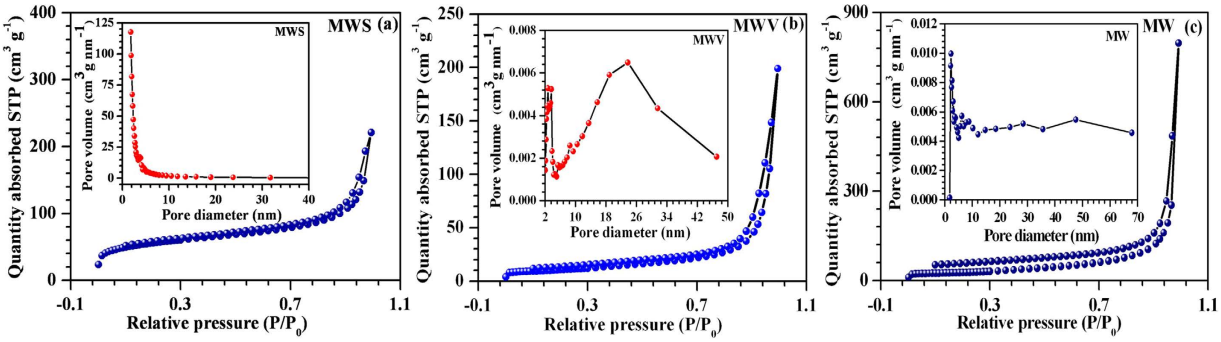

Figure 2. BET adsorption-desorption isotherms and pore size distribution for (**a**) MWS; (**b**) MWV; (**c**) MW sample.

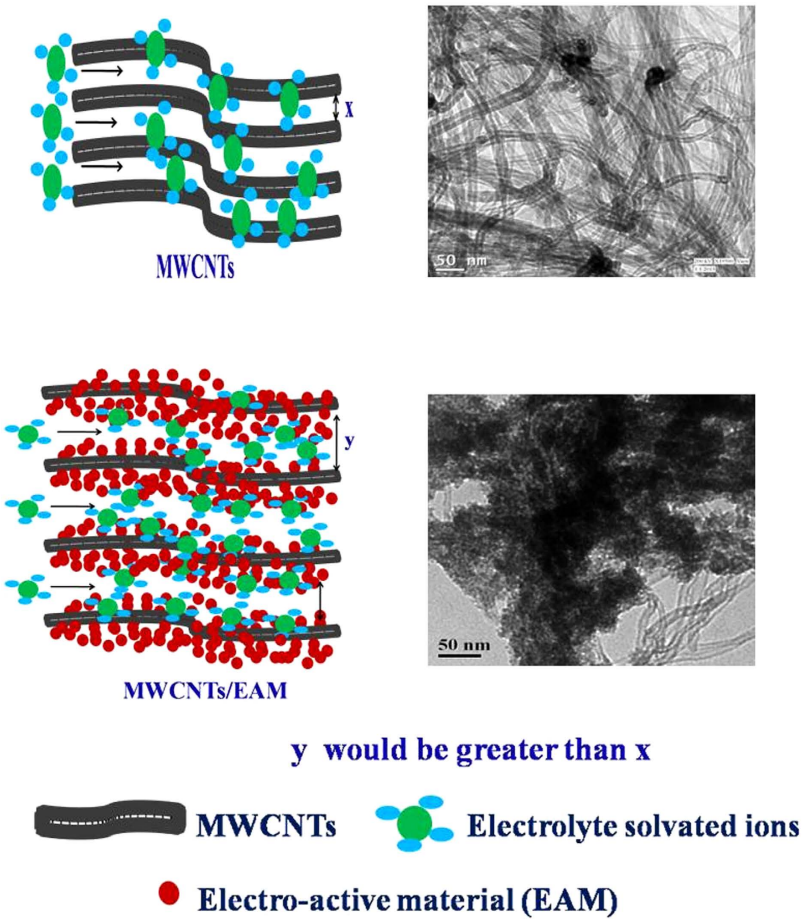

Figure 3. Theoretically conceptualized model to explain the opening of entangled carbon nanotubes as a result of composite formation.

the data, it could be inferred that the majority of the pores had dimensions <10 nm. Figure 2b,c shows similar isotherms obtained in MWV and MWCNTs (MW) samples, respectively. The Brunauer–Emmett–Teller (BET) surface areas for the MWS, MWV and MW samples were found to be ~187 $m^2 g^{-1}$, 37 $m^2 g^{-1}$ and 92 $m^2 g^{-1}$, respectively. The MWV composite exhibited pores located in the mesopores range ~2.7 to 23.6 nm. The formation of such mesoporous structure can be attributed to the opening of the entangled CNTs due to the presence of metal oxides and voids formed during the packing of the different crystallites. This is schematically shown in Fig. 3. Meso-porosity is a desirable attribute for supercapacitor electrode assemblies as it can provide increased number of channels for the diffusion of electrolyte ions leading to enhanced charge storage.

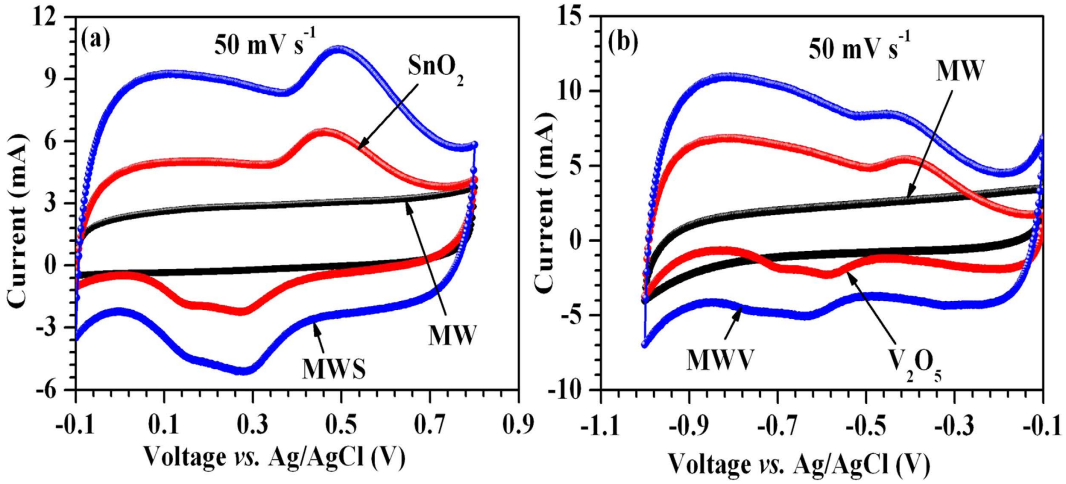

Figure 4. Synergistic effect between MWCNTs and (**a**) SnO_2; (**b**) V_2O_5.

Individual electrochemical performance and charge-balancing. For sustainable device operation, ensuring charge balance condition is essential. Therefore, individual electrochemical performances for all the active materials were investigated using a three-electrode system comprising a saturated KCl Ag/AgCl reference electrode and a Pt counter electrode. Figure 4a depicts the CVs for the MW, SnO_2 and MWS composite collected in the positive potential range at 50 mV s^{-1}. A rectangular shaped CV was observed for the MW sample while redox peaks were discernible with SnO_2 and MWS composite samples. The CV loop for MWS exhibited larger area (specific capacity ~218 F g^{-1}) in comparison to that observed for MW or SnO_2 nanoparticles alone (~29 F g^{-1} and ~136 F g^{-1}). This can be explained by knowing the fact that MWS had higher surface area, enhanced porosity and improved conductivity, that would lead to effective utilization of the inner bulk i.e., positive synergistic effect. The CV curves recorded in the negative potential range for MW, V_2O_5 and MWV composite are shown in Fig. 4b. MWV also showed superior charge storage capacity (242 F g^{-1}) in comparison to only MW or V_2O_5 (64 and 127 F g^{-1}, respectively).

Figure 5a shows the CV curves of MWS collected at different scan rates between −0.1 to 0.8 V. Nearly rectangular shaped CV curves with pronounced redox peaks were observed. These are linked to the intercalation/de-intercalation of electrolyte ions into the SnO_2 matrix ($SnO_2 + M^+ + e^- \leftrightarrow SnOOM$ where M^+ is the proton or electrolyte cation) and/or the redox reactions of the various functional groups present on the surface of MWCNTs[26–28]. In the composite material, MWCNTs provide the conducting pathways for the electron transfer while the SnO_2 nanoparticles control the redox reactions with the electrolyte ions. The uncovered surface of MWCNTs can also exhibit double layer capacitance due to the adsorption of the electrolyte ions. As a consequence of positive synergistic effect, a maximum specific capacitance of ~412 F g^{-1} could be achieved using MWS composite material at a scan rate of 5 mV s^{-1}. Equation (1) was used to calculate the specific capacitance (C):

$$C = \frac{1}{2msV}\int_{V_-}^{V_+} i(V)\,dV \tag{1}$$

where m is the mass of the active material excluding mass of the binder (with mass of positive electrode $m_+ = 1$ mg), s is the scan rate, V_- and V_+ represent the lower and upper voltage value of the voltage window range V, and $i(V)$ denotes the corresponding current response.

The specific capacitance values at 10, 20, 50, 75 and 100 mV s^{-1} were found to be ~348, 289, 218, 204 and 190 F g^{-1}, respectively. This shows good rate capability of MWS composite material with ~54% capacitance fade at a scan rate of 100 mV s^{-1}. The CVs at various scan rates for the MWV composite in the negative potential range (−0.1 to −1.0 V) was also recorded and is shown in Fig. 5b. Similar to the earlier case, nearly horizontal quasi-rectangular CVs were observed with sharp redox peaks. This can be attributed to the insertion/de-insertion of electrolyte cations into V_2O_5/VO_2 layered structures and/or redox reactions associated with surface functionality of the MWCNTs[29–31]. The positive synergistic effect between vanadium oxide and MW leads to a maximum specific capacitance of ~535 F g^{-1} at 5 mV s^{-1} scan rate.

The specific capacitance for MWV and MWS will be the sum of double layer (adsorption process) and pseudocapacitance (due to redox reaction, intercalation and diffusion inside the bulk active material). The variation of cumulated specific capacitance is shown in Fig. 5c. This is found to decrease linearly at a rate proportional to $v^{-1/2}$ (v is the scan rate). The deviation from the linearity at higher scan rates appears due to the reduced utilization of the active material. Therefore, these data points were excluded

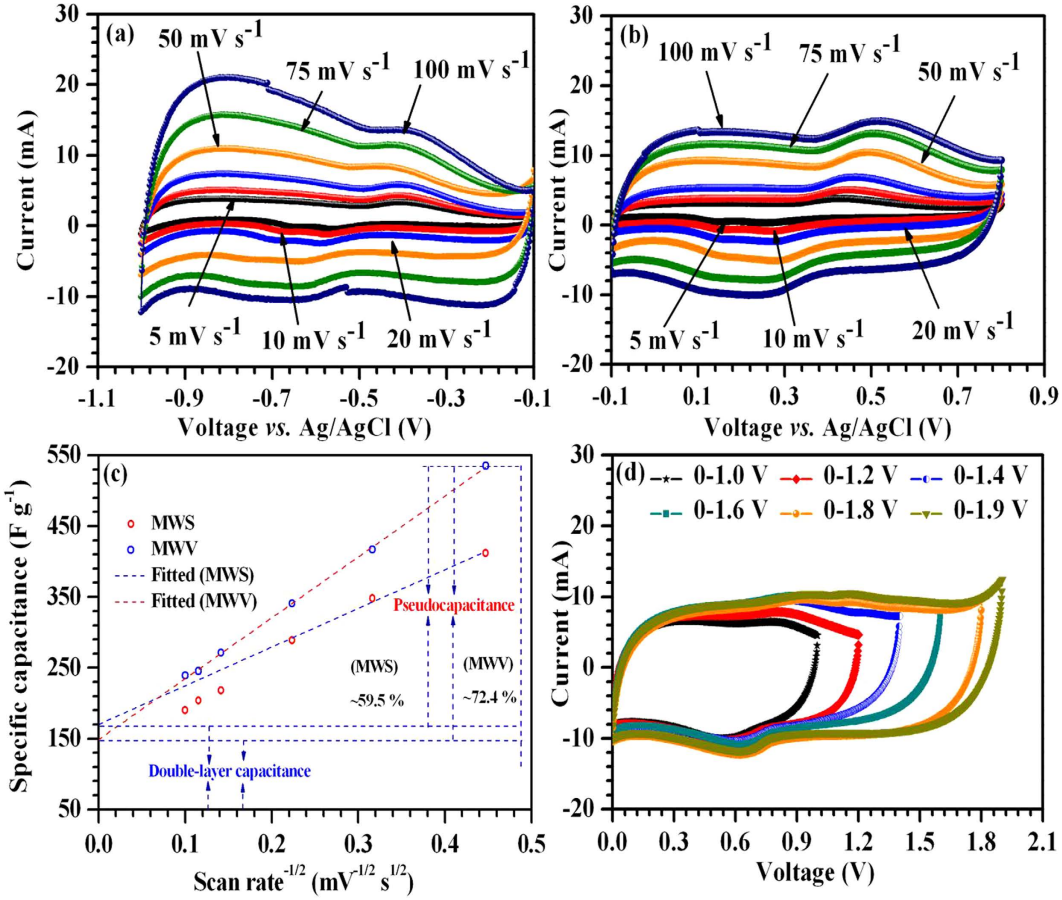

Figure 5. (**a,b**) Three electrode CV curves MWS and MWV, respectively; (**c**) quantification of double-layer and pseudocapacitance; (**d**) explaining stable voltage window for ASCs.

during the linear fitting. The extrapolation of fitted line towards $v^{-1/2} \rightarrow 0$ (infinite scan rate) gives the capacitance that is expected to originate electrostatically (adsorption) near the surface due to the slow pseudocapacitive processes[32]. The contribution of the electrode surface in the MWS (40.5%) is relatively high in comparison to MWV (27.6%). This can be attributed to relatively high surface area of the MWS composite which would result in a large interfacial contact region with the electrolyte.

The optimal mass ratio required for charge balancing the two electrodes was estimated using equation (2):

$$\frac{m_+}{m_-} = \frac{\Delta V\_C\_}{\Delta V_+ C_+} \tag{2}$$

where C_- and C_+ are the capacitances (in F g^{-1}) measured at the same scan rate, using the three electrode system, for negative and positive electrodes, respectively while ΔV_+ and ΔV_- denote the working potential window for the positive and negative electrodes, respectively. The required mass ratio for positive and negative electrode material (m_+/m_-) was thus estimated as 1.3 at 5 mV s^{-1}.

Electrochemical performance of asymmetric devices. ASCs were fabricated using the MWS and MWV electrodes (with $m_+ = 1.3$ mg and $m_- = 1$ mg), Whatman glass fiber paper separator (pre-soaked in electrolyte) and 0.5 mol L^{-1} Li_2SO_4 aqueous electrolyte. The CV curves for the device were recorded in different voltage ranges but at a fixed scan rate of 50 mV s^{-1}. The observed data are shown in Fig. 5d. The ASC exhibited quasi rectangular-shaped CV curves up to 1.8 V with redox peaks but no signature of H_2/O_2 evolution. However, in 1.9 V voltage window, there was a sharp rise in the current which indicated the release of H_2 or O_2 gases. Using the optimization experiments, stable operating voltage window for our fabricated ASC was inferred as 1.8 V. Although, high hydration energy of the used neutral electrolyte predicts ~1.6–2.2 V for water electrolysis into gases, the operating voltage window was limited to 1.8 V in the present case. This could be explained by taking into account the difference between the work functions of the used metal oxides. More detailed discussion is given later.

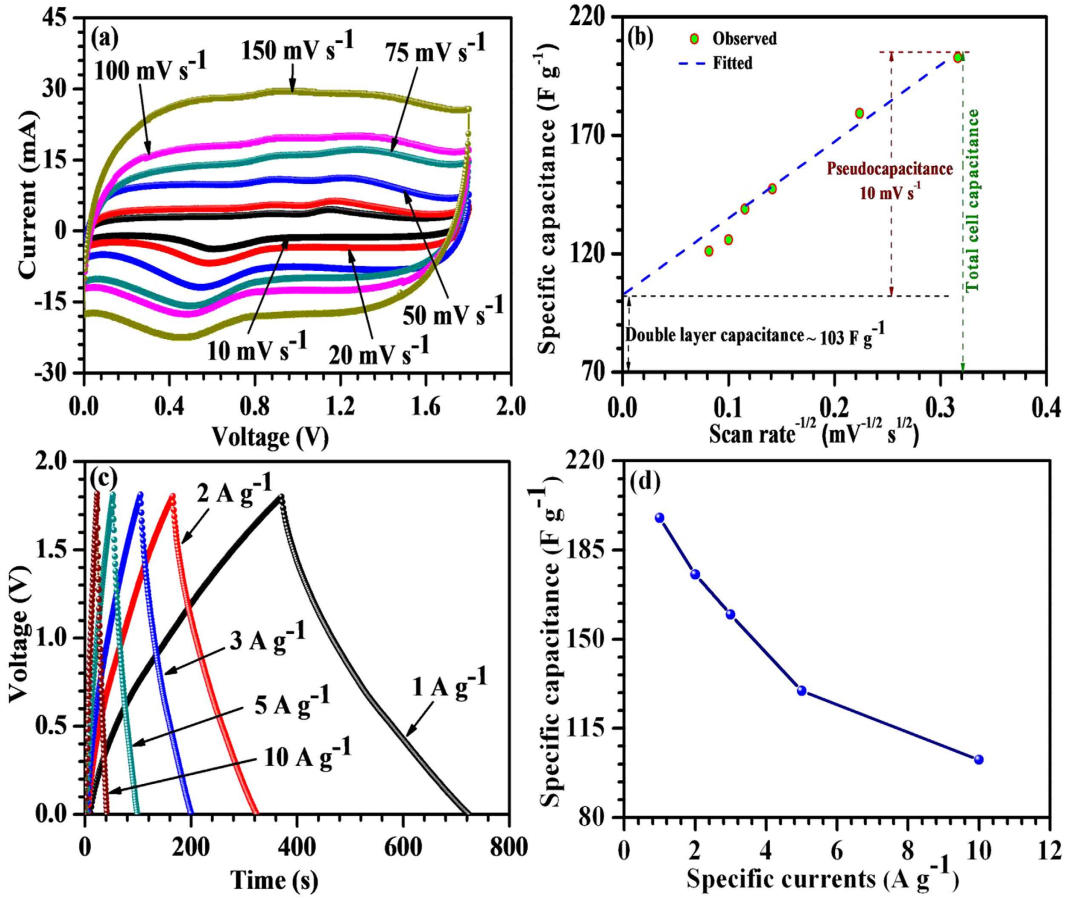

Figure 6. (**a**) Two electrode CV curves; (**b**) quantification of double-layer and pseudocapacitance; (**c**) galvanostatic charge-discharge curves; (**d**) rate capability for ASCs.

Figure 6a shows a series of CV measurements performed within 0–1.8 V at 10, 20, 50, 75, 100 and 150 mV s^{-1} scan rates for ASCs. Nearly rectangular-shaped CVs were observed at each scan rate with redox peaks. These peaks were more pronounced at small scan rates, which indicated convoluted contribution from double layer capacitance as well as pseudocapacitance. The nearly horizontal nature of these CVs indicates a small contribution from the equivalent series resistance of the ASCs[33]. The contribution from the electrode surface in ASCs operated at 10 mV s^{-1} was found to be ~50%, as shown in Fig. 6b. The contribution from the bulk of the electrodes decreased at higher scan rates indicating underutilized inner bulk of the active materials. The observed galvanostatic charge-discharge curves at specific currents of 1, 2, 3, 5 and 10 A g^{-1} in the voltage range 0–1.8 V are shown in Fig. 6c. Nearly symmetrical triangular-shaped charge/discharged curves confirmed the capacitive behavior. The non-linearity in the discharge curves reaffirmed the presence of pseudocapacitance as well as double layer capacitance in the convoluted cell capacitance. The specific capacitance values at 1, 2, 3, 5 and 10 A g^{-1} were found to be ~198, 175, 160, 130 and 103 F g^{-1}, respectively. These values were calculated using the equation (3):

$$C_s = \frac{It_d}{m(V - IR)} \tag{3}$$

where C_s is the total cell capacitance (in F g^{-1}), I is the specific current, m is the total mass of both the active materials excluding binder (i.e., $m_+ + m_- = 2.3$ mg), t_d is the discharge time, V represents the stable operating voltage window and 'IR' is the measure of ohmic drop. It can be seen from Fig. 6d that ASCs demonstrated good rate capability with ~52% capacitance retention at 10 A g^{-1}. The specific energy and power are estimated using the equations (4) and (5):

$$E = \tfrac{1}{2} C_s V^2 \tag{4}$$

$$P = E/t \tag{5}$$

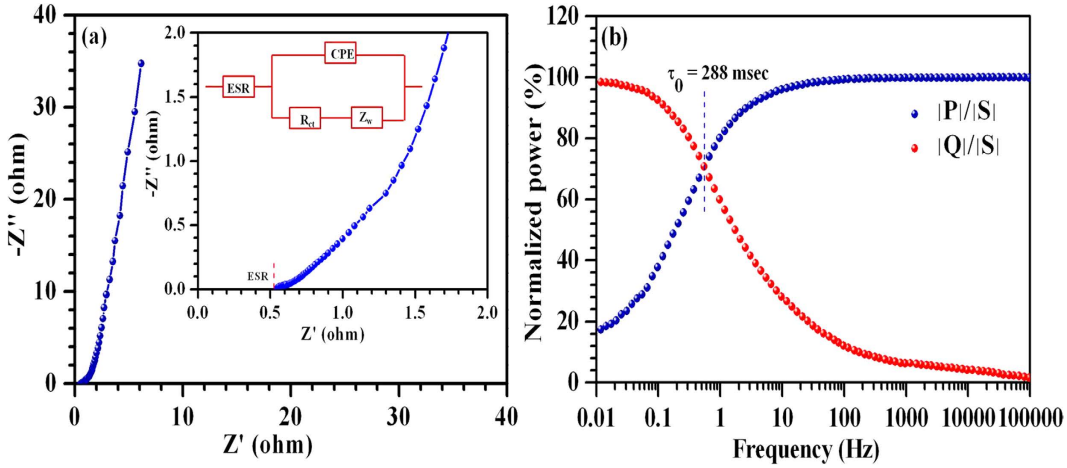

Figure 7. (**a**) Typical Nyquist plot and an equivalent circuit; (**b**) complex power analysis for ASCs.

where *E, C*$_s$*, V, P* and *t* stands for specific energy (mass normalized energy), specific capacitance, discharging voltage window excluding ohmic drop, specific power released and the discharge time, respectively.

The maximum specific energy obtained for the fabricated ASCs was ~89 Wh kg^{-1} at a specific power of ~903 W kg^{-1}. The ASCs retain specific energy of ~46 Wh kg^{-1} at a specific current of 10 A g^{-1} while specific power reaches to ~9,002 W kg^{-1}.

Figure 7a shows the typical Nyquist plot observed for the fabricated ASCs in 1 mHz-100 kHz frequency range using a small ac perturbation of amplitude 5 mV. This plot can be subdivided into low and high frequency regions. The vertical rise in impedance value, at low frequencies, indicated good capacitive behavior. The region at 45°, in the moderate frequency region, is attributed to Warburg impedance arising due to frequency dependence of electrolyte ion diffusion inside the pores. The high frequency region possesses a small semicircle as manifested in the inset. This is indicative of the small charge transfer resistance at the electrolyte/electrode interfaces. The observed Nyquist plot can be represented by an equivalent circuit as shown in the inset of Fig. 7a. ESR is the equivalent series resistance comprising resistance of the electrode materials, electrolytes, current collectors and contact resistance (~0.55 Ω for the present case), CPE is the constant phase element, R_{ct} is the charge transfer resistance and Z_w is the Warburg impedance.

Another figure of merit for the supercapacitors is the relaxation time constant (τ_0), which can be estimated by analyzing the power dissipated into the system. Figure 7b shows the variation of real and imaginary part of the normalized complex power $S(\omega)$ as a function of frequency, which were calculated using equations (6–8):

$$P(\omega) = \omega C''(\omega) \left|\Delta V_{rms}\right|^2 \tag{6}$$

$$Q(\omega) = -\omega C'(\omega) \left|\Delta V_{rms}\right|^2 \tag{7}$$

$$S(\omega) = P(\omega) + jQ(\omega) \tag{8}$$

where $\left|\Delta V_{rms}\right|^2 = \Delta V_{max}/\sqrt{2}$ (V_{max} is the maximum amplitude of the applied ac perturbation) and j is imaginary number while the angular frequency ω is equal to $2\pi f$. The C' and C'' represent the real and imaginary part of the complex capacitance and calculated using following relations (equation (9) and (10)):

$$C'(\omega) = -Z''(\omega)/\{\omega |Z(\omega)|^2\} \tag{9}$$

$$C''(\omega) = Z'(\omega)/\{\omega |Z(\omega)|^2\} \tag{10}$$

where Z' and Z'' represents real and imaginary parts of the complex impedance Z. The normalized powers corresponding to phase angle of 45° converge at a frequency f_0 ~552 mHz (known as relaxation frequency). Below this frequency, capacitive behavior supersedes the resistive behavior before reaching a pure capacitive characteristic at low frequency ~10 mHz. The relaxation time constant τ_0 (equal to $1/2\pi f_0$) for the as-fabricated ASCs was found to be ~0.3 s. This clearly indicated fast charging-discharging capability of the fabricated ASCs. Cyclic stability is also essential for industrial applications of ASCs. Therefore, the fabricated ASCs were cycled at 2 A g^{-1}. The data indicated only 4.2% capacitance fade

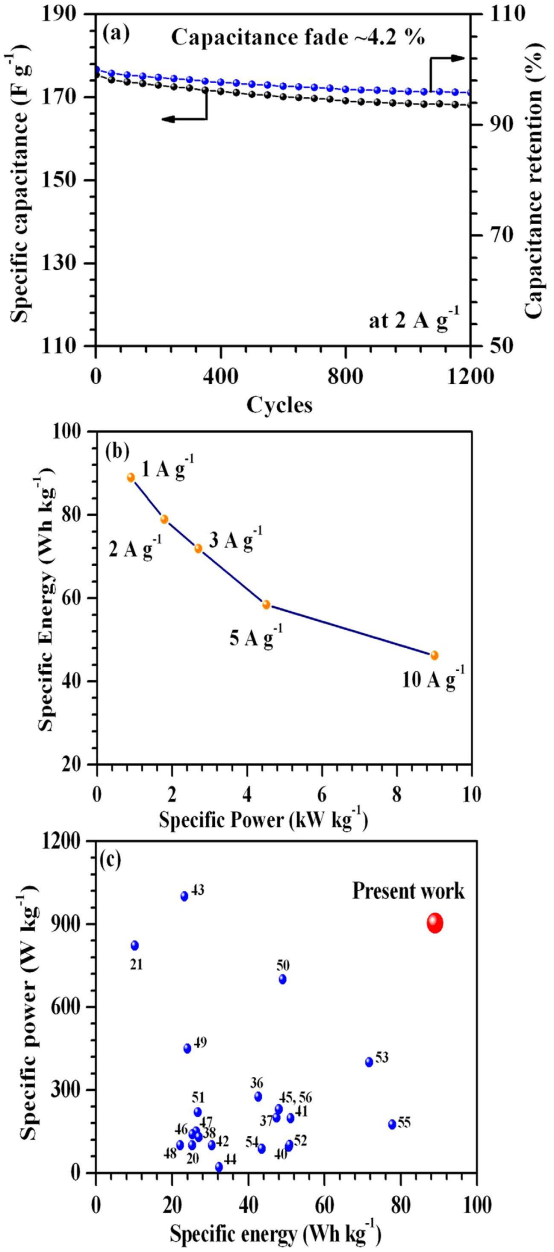

Figure 8. (**a**) cycling stability; (**b**) Ragone plot; (**c**) performance comparison for the fabricated ASCs.

after 1200 cycles (see Fig. 8a). The presence of oxygen vacancies can lead to an improved intercalation capacity and cyclic stability of V_2O_5 structures and ultimately, to an improved cyclic stability of ASCs[34,35].

The Ragone plot (specific energy versus power plot) for fabricated ASCs at different specific currents is given in Fig. 8b. The obtained specific energy and power values were compared with those reported previously for ASCs based on aqueous electrolyte. This is graphically shown in Fig. 8c[20,21,36–56]. It is clear from Fig. 8c that our ASCs exhibit much superior specific energy whilst maintaining high specific power. The above results establishes the relevance of using these metal oxides/MW composites for fabricating high-performance ASCs in aqueous electrolytes. A more detailed comparison with structures of the fabricated ASCs, used electrolyte, operating voltage window and cyclic stability is also given in supplementary Table S1.

Discussion

The electrode potential can be defined against a reference electrode (known as electrochemical scale) or with respect to electron energy at rest in vacuum (known as physical scale)[57–59]. When it is defined on a physical scale, the working voltage window of an electrochemical cell is given by:

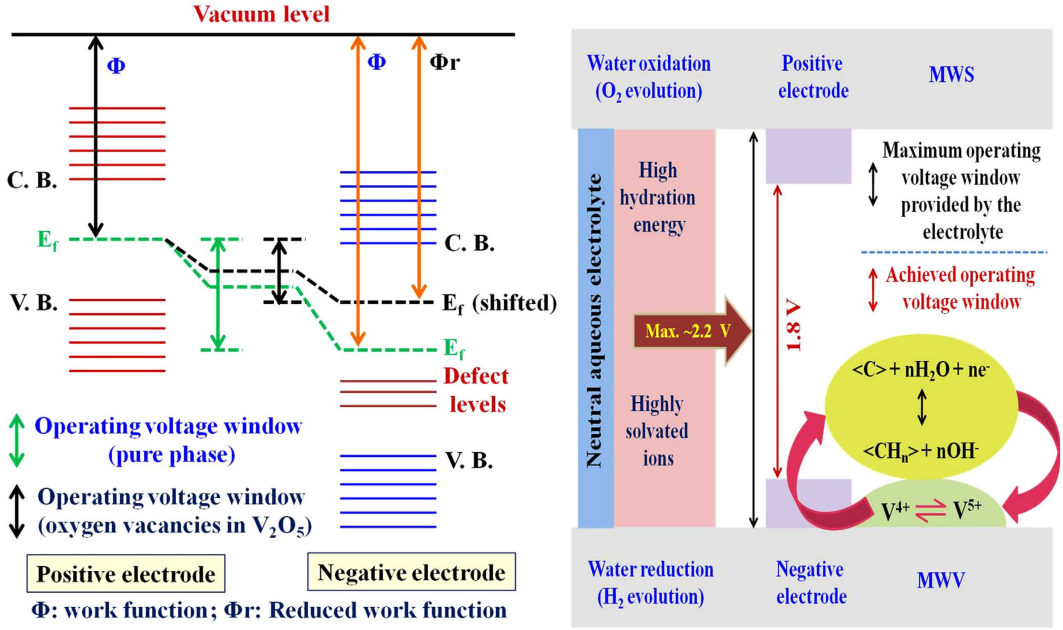

Figure 9. Energy band diagram explaining the stable and expanded operating voltage window achieved in the present ASCs.

$$E = E_0 + \Delta E_1 + \Delta E_2 = (\omega^{\beta} - \omega^{\alpha}) N_A/F + E_1 + E_2 \quad (11)$$

where ω^{α} and ω^{β} represents the work functions while ΔE_1 and ΔE_2 denotes the potentials of positive and negative electrodes, respectively and N_A stands for Avogadro's constant[36]. In an ASC, the difference in the work function of the two metal oxides widens the operating voltage window beyond the decomposition energy of electrolyte because $\omega^{\beta} - \omega^{\alpha} \neq 0$ and $E_1 \approx -E_2$ for correctly charge balanced electrodes. For the present case, work function difference between SnO_2 and V_2O_5 was ~2.35 eV, similar to that reported elsewhere[36]. Therefore, the expected stable operating voltage window was 2.2 V. In the present case, the observed voltage window of 1.8 V can be explained by the presence of oxygen vacancies in the V_2O_5 structures. Vanadium (V) oxide is a wide band gap oxide (d^0 oxide) which has a tendency to form oxygen vacancies. The formation of the O-vacancies gives rise to other phases (VO_2 for the present case) in addition to the V_2O_5 phase. This inference is supported by the XRD and XPS results for the MWV composite. The presence of the other VO_2 phase changes d^0-state of V_2O_5 to d^1-state and ultimately results in a reduced work function[60]. Thus, V^{5+}/V^{4+} phase with reduced work function forces water reduction at lower potentials for production and adsorption of atomic/nascent hydrogen on the MW surface. This results in a lower operating voltage than the predicted maximum achievable window (2.2 V). The modification in the band structure is schematically explained in Fig. 9.

Conclusions

The synergistic effect between the pseudocapacitive nanostructures of SnO_2 and V_2O_5 and carbon nanotubes lead to pronounced increase in the specific energy and power values delivered by the asymmetric supercapacitors. The fabricated asymmetric supercapacitors show superior electrochemical performance in comparison to those reported previously for ASCs in aqueous electrolytes. The charge balanced device returns the specific capacitance of ~198 F g^{-1} with corresponding specific energy of ~89 Wh kg^{-1} at 1 A g^{-1}. Such high values can be attributed to: (a) high specific surface areas of the MWS and MWV along with good porosity that induce large interfacial contact region between the electrode material and electrolyte, (b) the positive synergistic effect between MW and the used metal oxides (c) the use of a neutral aqueous electrolyte with highly solvated ions and (d) a large difference in the work function of the used metal oxides.

Methods

Materials used. Multiwall carbon nanotubes (MWCNTs) (ID 3–5 nm; OD 20–25 nm; length 20 μm and purity 95.0%) were purchased from Nanocyl (Belgium). Tin chloride ($SnCl_4.2H_2O$) and ammonium metavanadate (NH_4VO_3) were purchased from Loba chemicals Pvt. Ltd., India. Hydrochloric acid (HCl; 38%), isopropanol and ammonium hydroxide (25% ammonia solution) were purchased from Loba Chemie Pvt. Ltd., India. All the chemicals were used without further purification. Whatman glass microfiber filters (GF/C™; diameter 47 mm) were purchased from GE Healthcare UK Limited, UK.

Material synthesis and characterizations. Initially, functionalization of the MWCNTs (MW) was carried out by refluxing them in concentrated HNO_3 (69%) at 120 °C for 12 h. For the MWS composite, 200 mg functionalized MW were added in 300 ml de-ionized (DI) water and stirred overnight at room temperature to get homogenous dispersion. The solution of tin chloride (0.2 g $SnCl_4.2H_2O$ in 100 ml of DI water) with 3 ml of 38% HCl was then added to MW dispersion and heated at 90 °C for 12 h in an oil bath. Finally, product was collected by filtration followed by washing several times with DI water and finally dried overnight at 70 °C in a vacuum oven. To synthesize MWV composite, first, ammonium vanadate/MW was prepared by refluxing 200 mg functionalized MW and 25 g of V_2O_5 in 187 ml isopropanol and 35 ml of 4.2 M NH_4OH aqueous solution at 70 °C for overnight. The product was obtained by filtration followed by washing several times with DI water and drying at 60 °C for 36 h in a vacuum oven. MWV was obtained by heating the product thus obtained at 500 °C for 10 h in N_2 environment. Pure SnO_2 and V_2O_5 were also synthesized by following the same procedures.

Powder X-ray diffraction (XRD) patterns were collected for the synthesized materials using PAN Analytical diffractometer with Cu-Kα radiation at wavelength 1.5406 Å in 2θ range 15–70°. For morphological study, the samples were subjected to field emission scanning electron microscopy (SEM CARL ZEISS SUPRA 40) and high resolution transmission electron microscopy (TEMFEI-TECHNAI G220S-Twin operated at 200 kV). X-ray photoelectron spectroscopy (XPS) measurements were carried out with the help of PHI 5000VERSAProbe II X-ray photoelectron spectrometer having Al-Kα as incident photon energy. Thermogravimetric analysis (TGA) was performed in O_2 environment at 10 °C min^{-1} using NETZSCH STA 409 PC/PG thermal analyzer. Fourier transform infrared spectroscopy (FTIR) spectra were collected using Spectrum BX FTIR (Perkin Elmer version 5.3). The Brunauer-Emmett-Teller (BET) surface area and porosity were measured by analysing adsorption-desorption isotherms obtained from Micromeritics Gemini V Model 2365 and Gemini VII Model 2390t.

Device fabrication and electrochemical characterizations. To prepare electrodes, slurry was prepared using 95% of the active materials (i.e., MW, MWS, SnO_2, V_2O_5 or MWV) and 5% polyvinylidene fluoride (PVDF) in 50 ml acetone and heated at 100 °C to get homogeneous and stable slurry. Then, slurry was drop casted on graphite sheet (100 μm thick; area ~1 cm^2) to get desire mass loading. Finally, electrodes were dried at 100 °C before their use in device. Three electrode CV measurements were performed using a set-up provided by Metrohm Autolab comprising a reference electrode (Ag/AgCl; saturated KCl) and a counter electrode (Pt electrode). The mass of each active material used in three electrode CV measurements was ~1 mg. For the 3-electrode CVs of SnO_2, the starting potential is -0.1 V (*vs.* Ag/AgCl) and starting step of the CV measurement is positive sweep. However, in case of V_2O_5, the starting potential is -0.1 V (*vs.* Ag/AgCl) but the starting step of the CV measurement is negative sweep. The ASCs were fabricated by sandwiching a glass fibre paper (soaked in 0.5 M Li_2SO_4 aq. electrolyte) between two electrodes with required mass ratio ($m_+/m_- = 1.3$ with $m_+ = 1.3$ mg and $m_- = 1.0$ mg) as derived from charge balanced equation (2). The whole device is slightly pressed between two stainless-steel clamps. The electrochemical characterizations of ASCs were performed using a Metrohm Autolab (Galvanostat/Potentiostat) associated with Nova 1.10.1.9 software.

References

1. Wang, G., Zhang, L. & Zhang, J. A review of electrode materials for electrochemical supercapacitors. *Chem. Soc. Rev.* **41,** 797–828 (2012).
2. Simon, P. & Gagotsi, Y. Materials for electrochemical capacitors. *Nat. Mater.* **7,** 845–854 (2008).
3. Béguin, F., Presser, V., Balducci, A. & Frackowiak, E. Carbons and electrolytes for advanced supercapacitors. *Adv. Mater.* **26,** 2219–2251 (2014).
4. Demarconnay, L. *et al.* Optimizing the performance of supercapacitors based on carbonelectrodes and protic ionic liquids as electrolyte. *Electrochim. Acta* **108,** 361–368 (2013).
5. Liu, C., Li, F., Ma, L. P. & Cheng, H. M. Advanced materials for energy storage. *Adv. Mater.* **22,** E28–E62 (2010).
6. Reddy, A. L. M., Gowda, S. R., Shaijumon, M. M. & Ajayan, P. M. Hybrid nanostructures for energy storage applications. *Adv. Mater.* **24,** 5045–5064 (2012).
7. Khadke, P. K. & Krewer, U. Performance losses at H_2/O_2 alkaline membrane fuel cell. *Electrochem. Commun.* **51,** 117–120 (2015).
8. Xia, H., Meng, Y. S., Yuan, G., Cui, C. & Lu, Li. A symmetric RuO_2/RuO_2 supercapacitor operating at 1.6 V by using a neutral aqueous electrolyte. *Electrochem. Solid St.* **15,** A60–A63 (2012).
9. Wang, F. *et al.* Electrode materials for aqueous asymmetric supercapacitors. *RSC Adv.* **3,** 13059–13084 (2013).
10. Chandra, A., Roberts, A. J., Yee, E. L. H. & Slade, R. C. T. Nanostructured oxides for energy storage applications in batteries and supercapacitors. *Pure Appl. Chem.* **81,** 1489–1498 (2009).
11. Zhao, X., Sanchez, B. M., Dobson, P. J. & Grant, P. S. The role of nanomaterials in redox-based supercapacitors for next generation energy storage devices. *Nanoscale* **3,** 839–855 (2011).
12. Roberts, A. J. & Slade R. C. T. Birnessite nanotubes for electrochemical supercapacitor electrodes. *Energy Environ. Sci.* **4,** 2813–2817 (2011).
13. Zhang, Y., Li, L., Su, H., Huang, W. & Dong, X. Binary metal oxide: advanced energy storage materials in supercapacitors. *J. Mater. Chem. A* **3,** 43–59 (2015).
14. Devaraj, S., Gabriel, G. S., Gajjela, S. R. & Balaya, P. Mesoporous MnO_2 and its capacitive behavior. *Electrochem. Solid St.* **15,** A57–A59 (2012).
15. Roberts, A. J. & Slade R. C. T. Controlled synthesis of ε-MnO_2 and its application in hybrid supercapacitor devices. *J. Mater. Chem.* **20,** 3221–3226 (2010).
16. Lokhande, C. D., Dubal, D. P. & Joo, O. S. Metal oxide thin film based supercapacitors. *Curr. Appl. Phys.* **11,** 255–270 (2011).
17. Rakhi, R. B., Chen, W., Cha, D. & Alshareef, H. N. High performance supercapacitors using metal oxide anchored graphene nanosheet electrodes. *J. Mater. Chem.* **21,** 16197–16204 (2011).

18. Yu, G., Xie, X., Pan, L., Bao, Z. & Cui, Y. Hybrid nanostructured materials for high-performance electrochemical capacitors. *Nano Energy* **2,** 213–234 (2013).
19. Singh, A. & Chandra, A. Graphene and graphite oxide based composites for application in energy systems. *Phys. Status Solidi B* **250,** 1483–1487 (2013).
20. Cao, J. *et al.* High voltage asymmetric supercapacitor based on MnO_2 and graphene electrodes. *J. Electroanal. Chem.* **689,** 201–206 (2013).
21. Senthilkumar, S. T., Selvan, R. K., Ulaganathan, M. & Melo, J. S. Fabrication of Bi_2O_3||AC asymmetric supercapacitor with redox additive aqueous electrolyte and its improved electrochemical performances. *Electrochim. Acta* **115,** 518–524 (2014).
22. Wang, W., Hao, Q., Lei, W., Xia, X. & Wang, X. Graphene/SnO_2/polypyrrole ternary nanocomposites as supercapacitor electrode materials. *RSC Adv.* **2,** 10268–10274 (2012).
23. Raj, D. V., Ponpandian, N., Mangalaraj, D., Balamurugan, A. & Viswanathan, C. Electrochemical performance of SnO_2 hexagonal nanoplates. *Ionics* **20,** 335–346 (2014).
24. Boukhalfa, S., Evanoff, K. & Yushin, G. Atomic layer deposition of vanadium oxide on carbon nanotubes for high-power supercapacitor electrodes. *Energy Environ. Sci.* **5,** 6872–6879 (2012).
25. Chandra, A., Roberts, A. J. & Slade, R. C. T. Nanostructured vanadium oxide based systems: their applications in supercapacitors. *Int. J. Nanotechnology* **7,** 861–869 (2010).
26. Wu, M., Zhang, L., Wang, D., Xiao, C. & Zhang, S. Cathodic deposition and characterization of tin oxide coatings on graphite for electrochemical supercapacitors. *J. Power Sources* **175,** 669–674 (2008).
27. Li, F. *et al.* One-step synthesis of graphene/SnO_2 nanocomposites and its application in electrochemical supercapacitors. *Nanotechnology* **20,** 455602–455607 (2009).
28. Ng, K. C., Zhang, S., Peng, C. & Chen, G. Z. Individual and bipolarly stacked asymmetrical aqueous supercapacitors of CNTs/SnO_2 and CNTs/MnO_2 nanocomposites. *J. Electrochem. Soc.* **156,** A846–A853 (2009).
29. Pan, A. *et al.* Enhanced lithium-ion intercalation properties of coherent hydrous vanadium pentoxide-carbon cryogel nanocomposites. *J. Power Sources* **195,** 3893–3899 (2010).
30. Wang, Y. & Cao, G. Synthesis and enhanced intercalation properties of nanostructured vanadium oxides. *Chem. Mater.* **18,** 2787–2804 (2006).
31. Oh, Y. J. *et al.* Oxygen functional groups and electrochemical capacitive behavior of incompletely reduced graphene oxides as a thin-film electrode of supercapacitor. *Electrochim. Acta* **116,** 118–128 (2014).
32. Sankar, K. V. *et al.* Studies on the electrochemical intercalation/de-intercalation mechanism of $NiMn_2O_4$ for high stable pseudocapacitor electrodes. *RSC Adv.* **5,** 27649–27656 (2015).
33. Shaijumon, M. M., Ou, F. S., Ci, L. & Ajayan, P. M. Synthesis of hybrid nanowire arrays and their application as high power supercapacitor electrodes. *Chem. Commun.* 2373–2375 (2008).
34. Liu, D. *et al.* V_2O_5 xerogel electrodes with much enhanced lithium-ion intercalation properties with N_2 nnealing. *J. Mater. Chem.* **19,** 8789–8795 (2009).
35. Wang, H., Yi, H., Chen, X. & Wang, X. One-step strategy to three-dimensional graphene/VO_2 nanobelt composite hydrogels for high performance supercapacitors. *J. Mater. Chem. A* **2,** 1165–1173 (2014).
36. Chang, J. *et al.* Asymmetric supercapacitors based on graphene/MnO_2 nanospheres and graphene/MoO3 nanosheets with high energy density. *Adv. Funct. Mater.* **23,** 5074–5083 (2013).
37. Jiang, H., Li, C., Sun, T. & Ma, J. A green and high energy density asymmetric supercapacitor based on ultrathin MnO_2 nanostructures and functional mesoporous carbon nanotube electrodes. *Nanoscale* **4,** 807–812 (2012).
38. Cheng, Y., Zhang, H., Lu, S., Varanasi, C. V. & Liu, J. Flexible asymmetric supercapacitors with high energy and high power density in aqueous electrolytes. *Nanoscale* **5,** 1067–1073 (2013).
39. Chen, P., Shen, G., Shi, Y., Chen, H. & Zhou, C. Preparation and characterization of flexible asymmetric supercapacitors based on transition-metal-oxide nanowire/single-walled carbon nanotube hybrid thin-film electrodes. *ACS Nano* **4,** 4403–4411 (2010).
40. Tang, Z., Tang, C. & Gong H. A high energy density asymmetric supercapacitor from nano-architectured $Ni(OH)_2$/carbon nanotube electrodes. *Adv. Funct. Mater.* **22,** 1272–1278 (2012).
41. Fan, Z. *et al.* Asymmetric supercapacitors based on graphene/MnO_2 and activated carbon nanofiber electrodes with high power and energy density. *Adv. Funct. Mater.* **21,** 2366–2375 (2011).
42. Wu, Z. *et al.* High-energy MnO_2 nanowire/graphene and graphene asymmetric electrochemical capacitors. *ACS Nano* **4,** 5835–5842 (2010).
43. Gao, H., Xiao, F., Ching, C. B. & Duan, H. High-performance asymmetric supercapacitor based on graphene hydrogel and nanostructured MnO_2. *ACS Appl. Mater. Interfaces* **4,** 2801–2810 (2012).
44. Zhao, X. *et al.* Incorporation of manganese dioxide within ultraporous activated graphene for high-performance electrochemical capacitors. *ACS Nano* **6,** 5404–5412 (2012).
45. Wang, H. *et al.* Advanced asymmetrical supercapacitors based on graphene hybrid materials. *Nano Res.* **4,** 729–736 (2011).
46. Qu, Q. *et al.* A cheap asymmetric supercapacitor with high energy at high power: Activated carbon//$K_{0.27}MnO_2{\cdot}0.6H_2O$. *J. Power Sources* **195,** 2789–2794 (2010).
47. Zhang, J., Jiang, J., Li, H. & Zhao, X. S. A high-performance asymmetric supercapacitor fabricated with graphene-based electrodes. *Energy Environ. Sci.* **4,** 4009–4015 (2011).
48. Lei, Z., Zhang, J. & Zhao, X. S. Ultrathin MnO2 nanofibers grown on graphitic carbon spheres as high- performance asymmetric supercapacitor electrodes. *J. Mater. Chem.* **22,** 153–160 (2012).
49. Jin, W., Cao, G. & Sun, J. Hybrid supercapacitor based on MnO2 and columned FeOOH using Li_2SO_4 electrolyte solution. *J. Power Sources* **175,** 686–691 (2008).
50. Singh, A., Roberts, A. J., Slade, R. C. T. & Chandra, A. High electrochemical performance in asymmetric supercapacitors using MWCNT/nickel sulfide composite and graphene nanoplatelets as electrodes. *J. Mater. Chem. A* **2,** 16723–16730 (2014).
51. Mak, W. F. *et al.* High-energy density asymmetric supercapacitor based on electrospun vanadium pentoxide and polyaniline nanofibers in aqueous electrolyte. *J. Electrochem. Soc.* **159,** A1481–A1488 (2012).
52. Shao, Y., Wang, H., Zhang, Q. & Li, Y. High-performance flexible asymmetric supercapacitors based on 3D porous graphene/MnO_2 nanorod and graphene/Ag hybrid thin-film electrodes. *J. Mater. Chem. C* **1,** 1245–1251 (2013).
53. Wang, R. & Yan, X. Superior asymmetric supercapacitor based on Ni-Co oxide nanosheets and carbon nanorods. *Sci. Rep.* **4,** 3712–3720 (2014).
54. Zhou, C., Zhang, Y., Li, Y. & Liu, J. Construction of high-capacitance 3D CoO@polypyrrole nanowire array electrode for aqueous asymmetric supercapacitor. *Nano Lett.* **13,** 2078–2085 (2013).
55. Yan, J. *et al.* Advanced asymmetric supercapacitors based on $Ni(OH)_2$/graphene and porous graphene electrodes with high energy density. *Adv. Funct. Mater.* **22,** 2632–2641 (2012).
56. Li, Z. *et al.* Colossal pseudocapacitance in a high functionality–high surface area carbon anode doubles the energy of an asymmetric supercapacitor. *Energy Environ. Sci.* **7,** 1708–1718 (2014).
57. Trasatti, S. The absolute electrode potential: an explanatory note. *Pure & Appl. Chem.* **58,** 955–966 (1986).

58. Riess, I. & Vayenas, C. G. Fermi level and potential distribution in solid electrolyte cells with and without ion spillover. *Solid State Ionics* **159,** 313–329 (2003).
59. Tsiplakides, D. & Vayenas, C. G. Electrode work function and absolute potential scale in solid-state electrochemistry. *J. Electrochem. Soc.* **148,** E189–E202 (2001).
60. Wu, Q. H., Thissen, A., Jaegermann, W. & Liu, M. Photoelectron spectroscopy study of oxygen vacancy on vanadium oxides surface. *Appl. Surf. Sci.* **236,** 473–478 (2004).

Acknowledgements

Arvinder Singh acknowledges CSIR, India, for the award of Senior Research Fellowship. Amreesh Chandra acknowledges IIT Kharagpur for financial support under the SGIRG Research Grant. AC also acknowledges the funding received from IGSTC (DST, India) and MPG (Germany) under the Max Planck Partner Group Program.

Author Contributions

Both the authors contributed equally in the work reported in the manuscript. All authors reviewed the manuscript. Dr. Amreesh Chandra was also the supervisor of the work.

Additional Information

Supplementary information accompanies this paper at http://www.nature.com/srep

Competing financial interests: The authors declare no competing financial interests.

How to cite this article: Singh, A. and Chandra, A. Significant Performance Enhancement in Asymmetric Supercapacitors based on Metal Oxides, Carbon nanotubes and Neutral Aqueous Electrolyte. *Sci. Rep.* **5**, 15551; doi: 10.1038/srep15551 (2015).